



Article

Joint Analysis and Morphological Characterization of HFSWR Echo Properties during Severe Typhoon Muifa

Rong Wang, Zhe Lyu, Changjun Yu *, Aijun Liu and Taifan Quan

College of Information Science and Engineering, Harbin Institute of Technology, Weihai 264209, China; 21B905056@stu.hit.edu.cn (R.W.); lvzhehit@hit.edu.cn (Z.L.); liuaijun@hit.edu.cn (A.L.); quantf@hit.edu.cn (Q.T.)
* Correspondence: yuchangjun@hit.edu.cn

Abstract: Investigating the dynamic evolution process of the ocean and ionosphere in sudden sea conditions poses a challenging problem. To address this objective, this study utilizes actual data from high-frequency surface wave radar (HFSWR) to analyze, validate, summarize, and characterize the echo properties of the ocean and ionosphere during the severe Typhoon Muifa. By employing the short-time Fourier transform (STFT) method, the HFSWR ocean and ionosphere echoes stimulated by typhoon-induced gravity waves are observed, and the joint gravity wave features of the ocean and ionosphere echoes at different time scales are extracted. Additionally, the phase-space reconstruction method is employed to characterize the dynamical evolution of the joint gravity wave features in higher-dimensional space. Furthermore, the chaotic dynamics behavior of the joint gravity wave features is analyzed using the largest Lyapunov exponents. By combining the gravity wave features with chaotic dynamics, this study introduces a method to characterize the joint gravity wave features. The extraction of joint gravity wave features in HFSWR echoes stimulated by typhoons, along with the construction of a chaotic characterization scheme for the gravity wave features, provides an innovative approach and a solid technical foundation for studying the ocean and ionosphere using HFSWR under sudden sea conditions.

Keywords: ocean and ionosphere dynamic; radar; chaos; gravity waves; largest Lyapunov exponents



Citation: Wang, R.; Lyu, Z.; Yu, C.; Liu, A.; Quan, T. Joint Analysis and Morphological Characterization of HFSWR Echo Properties during Severe Typhoon Muifa. *Remote Sens.* **2024**, *16*, 267. <https://doi.org/10.3390/rs16020267>

Academic Editor: Massimiliano Pieraccini

Received: 20 October 2023
Revised: 27 December 2023
Accepted: 6 January 2024
Published: 10 January 2024



Copyright: © 2024 by the authors. Licensee MDPI, Basel, Switzerland. This article is an open access article distributed under the terms and conditions of the Creative Commons Attribution (CC BY) license (<https://creativecommons.org/licenses/by/4.0/>).

1. Introduction

The ocean and ionosphere are crucial components of the solar–terrestrial space environment. They form a system encompassing the near-Earth sea and air environment, which is significant for human understanding of our natural surroundings [1].

Gravity waves are the carriers of energy and provide kinetic energy transport between the ocean and ionosphere, playing a vital role in the dynamic relationship between the ocean and ionosphere. Energetic atmospheric events at sea, such as typhoons, tsunamis, and thunderstorms, result in energy dissipation in the ocean–ionosphere system, causing it to deviate from its expected equilibrium state. Among these, gravity waves excited by typhoons, as the primary carriers of energy transmission, cause the coupling of momentum and energy. This coupling significantly impacts the energy and momentum fluxes between the ocean and the ionosphere. Thus, examining the intricate dynamics between the ocean and the ionosphere during intense maritime events emerges as a novel scientific challenge in oceanic and ionospheric information acquisition [2]. According to Sorokin, Isaev et al., an analysis of satellite observations during typhoons at low latitudes revealed an increase in the intensity of the ionospheric electric field during typhoon transit [3,4]. Back in 1960, Hines and colleagues suggested utilizing gravity wave theory to explain how violent weather events like typhoons, thunderstorms, and tornadoes can cause disturbances in the ionosphere [5]. A collaborative study by Xiao and colleagues discovered that the ionosphere experiences a wave-like disturbance (sinusoidal quasi-periodic fluctuations) transition from high to low frequencies, the researchers reached this conclusion based on their analysis of

high-frequency Doppler records and typhoon data [6,7]. Yang et al. could also observe the quasi-periodic sinusoidal “S” pattern of traveling ionospheric disturbances (TIDs) in the ionospheric echoes by simulating HF-SWR typhoon data [8]. TIDs are typically generated by the interaction of gravity waves from neutral atmospheric structures with the ionosphere. There are two types of TIDs: large-scale and mesoscale. Large-scale TIDs have a horizontal phase velocity of approximately 400–1000 m/s, a period above 60 min, and a horizontal wavelength greater than 1000 km. Mesoscale TIDs have a horizontal phase velocity of less than 300 m/s, and their period falls between 10 and 60 min. Additionally, their horizontal wavelength spans several hundred kilometers [9]. In summary, gravity waves triggered by typhoons can reach the ionosphere, leading to the occurrence of TIDs. TIDs cause high-frequency Doppler perturbations that exhibit a distinct S-shaped distribution. Furthermore, there is a clear physical link between typhoons and the ionosphere.

High-frequency surface wave radar (HF-SWR) is widely utilized in maritime applications for over-the-horizon target detection [10–12] and ocean remote sensing [13–16] due to its unique capabilities. Furthermore, there have been significant advances in HF-SWR ionospheric-sounding research in recent years [17,18]. In light of current research on HF-SWR, there is a desire to further explore the complex dynamics of the ocean–atmosphere–ionosphere system under sudden changes in sea state, which presents an intriguing scientific challenge [19,20]. Chen et al. [21] utilized a mathematical model of the HF-SWR ionosphere to observe that TIDs can lead to electron density fluctuations, which cause additional Doppler effects because of the HF wave reflection height shift. During a fluctuation cycle of 45 min, the height of ionospheric reflection experiences a variation of 10%. It has been shown that simulations of TIDs at an altitude of 350 km demonstrate that HF-SWR ionospheric echoes experience an additional Doppler shift, leading to periodic fluctuations in both the azimuthal angle of the ionospheric echoes and the reflection height. Moreover, TIDs induce swift phase alterations in the radar signal, leading to a corresponding Doppler spread. Li et al. [22] validated the feasibility of using HF-SWR ionospheric echoes to detect typhoons. Chung et al. [23] utilized high-frequency surface wave radar (HF-SWR) range-Doppler (RD) spectroscopy to investigate the variations in ionospheric clutter during typhoons. The study revealed significant changes in the morphology of ionospheric clutter, with an increase in the proportion of strip-like clutter when Typhoon Soulik approached Taiwan. Regarding the possible physical mechanism, it is suggested that the lower atmospheric disturbances generated by the typhoon may propagate to the ionospheric heights in the form of acoustic-gravity waves, leading to instability in the ionosphere and plasma. Zhou et al. [24] utilized the OSMAR-S radar to analyze ionospheric echo data for extended periods of 24 h and short periods of around 6 min, they identified a clear superposition pattern of multiple continuous “S-shaped” time–frequency components and a fuzzy superposition pattern of multiple continuous time–frequency components. The research methodology outlined in [24] offers valuable insights for this study in HF-SWR.

As mentioned earlier, studies on the ionosphere are commonly conducted using a single observation time scale, limited to time, time–frequency, distance, or Doppler domains. The connection between typhoons, the ionosphere, and oceans must be considered, which may improve access to information and make it more comprehensive. The content of this manuscript is summarized as follows:

- This manuscript delineates the identification of joint gravity wave signatures observed in the HF-SWR ocean and ionosphere echoes. It also compares the variations in these signatures before and after the typhoon enters the detection range of HF-SWR, using time–frequency analysis and 2D localized methods.
- Furthermore, the evolution of the gravity wave signatures of the HF-SWR echoes is quantitatively characterized by reconstructing the chaotic attractor.

- Then, this study proposes a chaotic characterization scheme for HFSWR joint gravity wave signatures based on the largest Lyapunov exponents.
- The experimental results corroborate the validity and application extension of the novel proposed gravity wave pattern characterization scheme.

This manuscript utilizes data from HFSWR during Typhoon Muifa to analyze and describe the dynamic behavior of HFSWR echoes caused by typhoon-induced gravity waves, focusing on different time scales for the first time. This approach introduces an innovative perspective and furnishes robust technical backing to the domain of HFSWR ocean and ionosphere research during severe maritime occurrences.

2. Introduction to Typhoon Periods and Information

The data were recorded from the Weihai HFSWR station in Shandong Province on 16 September 2022, from 02:00 to 17:00 Beijing time, during Typhoon Muifa. The radar parameters are shown in Table 1. The receiving and transmitting antenna arrays of the Weihai HFSWR station are shown in Figure 1.

Table 1. Radar parameters.

Parameter	Value
Location	37.37°N, 122°E
Operating frequency	4.90 MHz
Pulse recurrence interval	3.63 ms
Distance accuracy	3.7 km
Sampling frequency	400 kHz
Sampling time	16 September 2022 02:00–15:00



(a)



(b)

Figure 1. Weihai HFSWR station. (a) Receiving antenna array. (b) Transmitting antenna array.

Severe Typhoon Muifa was recognized by the Central Weather Bureau at 08:00 on 8 September 2022, as having formed in the northwest Pacific Ocean and gradually intensified, reaching its peak intensity on 11 September. Severe Typhoon Muifa made its third landfall in Qingdao, Shandong Province, at 0:00 on 16 September 2022, as a tropical storm [25]. Muifa entered the Bohai Strait at 8:00 and made its fourth landfall in Dalian, Liaoning Province, at around 12:40 [26]. The Central Weather Bureau stopped categorizing severe Typhoon Muifa at 20:00 on 16 September [27].

As shown in Figure 2, severe Typhoon Muifa entered the detection range of the Weihai HFSWR station at 05:00 on 16 September 2022, and left around 13:00.

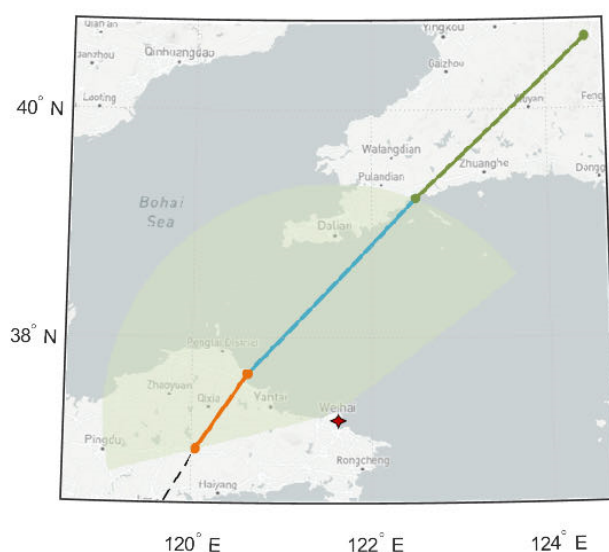


Figure 2. Severe Typhoon Muifa path diagram. The pentagram represents the location of the Weihai HFSWR station. The yellow and blue lines indicate the typhoon path segments within the detection range (16 September 5:00–13:00), and the blue line is the typhoon path segment located in the Bohai Strait. The green line segment indicates the typhoon path segment far from the detection range of the Weihai HFSWR station (16 September 13:00–15:00). The shaded area is the detection range of the Weihai HFSWR station. The normal direction of HFSWR operation points at Qinhuangdao.

Figure 3 shows the typical range-Doppler (RD) echo spectra of HFSWR before, during, and after the typhoon entered the detection range of the Weihai HFSWR station. During the severe Typhoon Muifa, the RD spectrum collected at the Weihai HFSWR station showed significant changes in the HFSWR echoes, as depicted in Figure 3. The altitude of ionospheric (F-layer) echoes drops from about 300 km to below 200 km, and there is no discernible pattern in Figure 3. In Figure 3a, the first-order spectrum of the ocean echo exhibits a noticeable Doppler frequency shift before the typhoon enters the detection range of the HFSWR Weihai station. After the typhoon enters the detection range of the HFSWR Weihai station, the Doppler shift of the first-order spectrum of the ocean echoes is opposite to that shown in Figure 3a, and the detection distance of the first-order spectrum of the ocean echoes increases. It is noted that the first-order spectrum of the ocean echoes produces a distinct S-shaped shift in the Doppler frequency dimension after leaving the detection range of the HFSWR Weihai station. The 'distinct S-shaped shift in the Doppler frequency' is mentioned only in the hope of providing some data observational material for future HFSWR typhoon warnings. The ocean echo's left side of the first-order spectrum is larger than the right when the typhoon moves near the HFSWR Weihai station. Conversely, the left side of the first-order spectrum is weaker than the right side when the typhoon is moving away from the HFSWR Weihai station. This phenomenon is related to the path of the typhoon. Thus far, the information obtained from the RD echo spectra is somewhat broad, necessitating the exploration of more refined qualitative and quantitative methods to elucidate the dynamic behaviors of oceanic echoes and ionospheric clutter during typhoons.

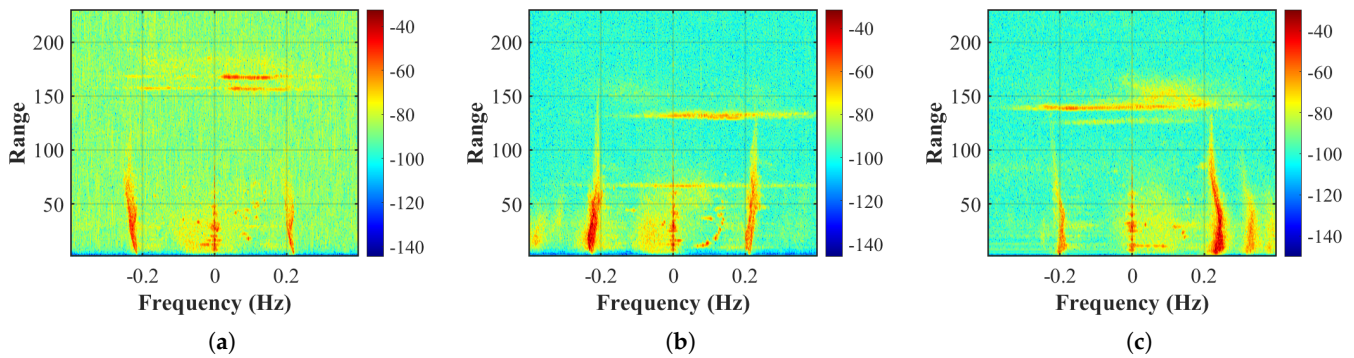


Figure 3. RD spectrum during severe Typhoon Muifa. (a) 16 September 02:00: RD spectrum with a straight-line distance of about 177 km from the Weihai HFSWR station. The typhoon's center is located on land in Qingdao, which is beyond the detection range of the HFSWR Weihai station. (b) 16 September 09:00: RD spectrum with a straight-line distance of about 88 km from the Weihai HFSWR station. The typhoon's center is located in the Bohai Strait, which is within the detection range of the HFSWR Weihai station. (c) 16 September 15:00: RD spectrum with a straight-line distance of about 270 km from the Weihai HFSWR station. The typhoon's center is located in Dalian, which is beyond the detection range of the HFSWR Weihai station.

3. Experimental Analysis

3.1. Analysis of HFSWR Ocean and Ionosphere Echoes

HFSWR ocean and ionosphere echoes are influenced by gravity waves generated by typhoons, resulting in distinctive signatures. In this section, the dynamical properties of ocean and ionosphere echoes during typhoons are found at different time scales, the interconnections and their trends are further analyzed using diverse quantitative methods, and the generality of the newly found properties is further verified.

The mathematical expression of the short-time Fourier transform (STFT) [28] is

$$X(t, f) = \sum_{T=-\infty}^{\infty} s(t)\omega(n-t)e^{-ift}, \quad (1)$$

where $s(t)$ represents the radar time-domain signal, and $\omega(t)$ is the window function with n sample offsets. $X(t, f)$ is a two-dimensional function of time t and frequency f . The time–frequency distribution is $S(t, f) = |X(t, f)|^2$.

The reconstructed phase-space trajectory can reflect the evolutionary law of the system to a certain extent [29]. The primary goal of phase-space reconstruction is to minimize the correlation among the elements of the reconstructed time series while preserving the original sequence's dynamic characteristics. In other words, phase-space reconstruction aims to preserve comprehensive information while eliminating local irrelevance. The mathematical description of the autocorrelation function is

$$C(\tau) = \lim_{t \rightarrow \infty} \int_{-\frac{\tau}{2}}^{\frac{\tau}{2}} s(t)^* s(t + \tau) dt. \quad (2)$$

The autocorrelation function $C(\tau)$ is plotted against the delay time τ using the observed data to determine the appropriate τ for the phase-space reconstruction. Once the autocorrelation function $C(\tau)$ drops to $1 - 1/e$ of its initial value, the delay time τ is determined. Taking Figure 4 as an example, the delay time τ is 12.

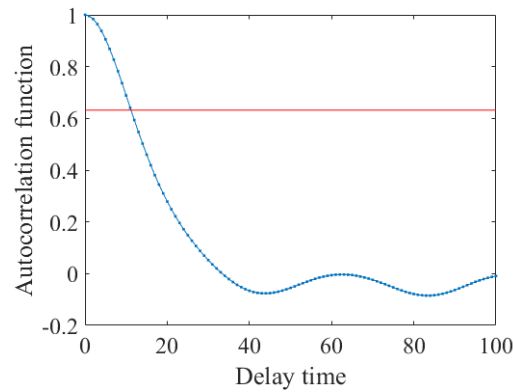


Figure 4. An example of using the autocorrelation method to find the time delay τ .

After the selected delay time, this paper utilizes the false nearest neighbors (FNNs) approach [30] to determine the embedding dimension m . In the d -dimensional phase space,

$$\vec{s}(i) = (s(i), s(i + \tau), \dots, s(i + (d - 1)\tau)), \tag{3}$$

and there exists a nearest neighbor point $\vec{s}^{NN}(i)$. The distance is defined as

$$R_d^p(i) = \|\vec{s}(i) - \vec{s}^{NN}(i)\|_p. \tag{4}$$

p is a norm value, usually taken as 2. When the number of dimensions increases from d to $d + 1$, then

$$R_{d+1}^p(i) = R_d^p(i) + \|\vec{s}(i + \tau d) - \vec{s}^{NN}(i + \tau d)\|_p, \tag{5}$$

$$a_1(i, d) = \frac{\|\vec{s}(i + \tau d) - \vec{s}^{NN}(i + \tau d)\|_p}{R_d^p(i)}. \tag{6}$$

If $a_1(i, d) > R_r$, $\vec{s}^{NN}(i)$ is the nearest neighbor point of the $\vec{s}(i)$, R_r is the customized threshold. To determine the optimal embedding dimension m , the proportion a_1 of false nearest neighbors is calculated based on the minimum value of d . Then, d is gradually increased until the proportion a_1 of false nearest neighbors is less than 5%. At this point, d becomes the optimal embedding dimension m . Figure 5 shows that the optimal embedding dimension m is 3.

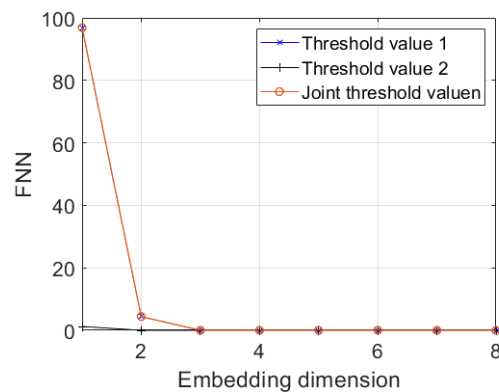


Figure 5. An example of false nearest neighbors method to find embedding dimension m .

The radar time series $s(i, f), i = [1, n]$ at the frequency f is reconstructed as the phase space \vec{y} , n represents the length of the time series.

$$\begin{cases} \vec{y}(1) = \vec{s}(1) = (s(1), s(1 + \tau), \dots, s(1 + (m - 1)\tau)) \\ \vec{y}(2) = \vec{s}(2) = (s(2), s(2 + \tau), \dots, s(2 + (m - 1)\tau)) \\ \dots \\ \vec{y}(i) = \vec{s}(i) = (s(i), s(i + \tau), \dots, s(i + (m - 1)\tau)) \\ \dots \\ \vec{y}(n - (m - 1)\tau) = \vec{s}[n - (m - 1)\tau] \\ = (s[n - (m - 1)\tau], \dots, s(n)) \end{cases} \quad (7)$$

$F(\cdot)$ is a one-step prediction system for phase-space attractors, the dynamical system modeled in a Euclidean space of embedding dimension m is

$$y_{i+1} = s(i + 1) = F(\vec{s}(i)) = F(\vec{y}(i)). \quad (8)$$

The Kolmogorov entropy K characterizes the attractor's disorganization level [31]. The Kolmogorov entropy is a concept in dynamical systems theory and information theory. The Kolmogorov entropy is the ratio of phase-space volumes between neighboring trajectories as the time interval approaches zero. The Kolmogorov entropy has applications in various fields. It provides insights into the behavior and predictability of chaotic systems, allows the classification of systems based on their complexity, and is used in information theory to quantify the amount of information generated by a stochastic process. The higher the Kolmogorov entropy, the more complex and uncertain the system is. In the reconstructed attractor time series, the separation of neighboring points on different trajectories is considered to follow an exponential rate. The time interval t_0 is required for two initially neighboring points to separate until the distance between them becomes more significant than l_0 , l_0 represents the specified maximum interpoint distance. So, the exponential distribution function $C(t_0)$ is defined as

$$C(t_0) \approx e^{-Kt_0}, \quad (9)$$

$$C(b) = e^{-KbT}, b = 1, 2, 3, \dots, M, \quad (10)$$

where T denotes the reciprocal of the sampling frequency.

The probability P of finding a distance bigger than l_0 after exactly b interpoint distances is

$$P(b) = C(b - 1) - C(b) = (e^{KT} - 1)e^{KbT} \quad (11)$$

The log-likelihood function $L(k)$ describes obtaining a sample (b_1, b_2, \dots, b_M) from a random sampling of M pairs of independent points on an attractor.

$$L(k) = \ln(P(b_1, b_2, \dots, b_M; k)) = M * \ln(e^k - 1) - k \sum_{i=1}^M b_i, \quad (12)$$

$$k = KT, \quad (13)$$

make

$$\frac{\partial L(k)}{\partial k} = 0, \quad (14)$$

then, the maximum likelihood estimate of the Kolmogorov entropy K_{ML} is calculated as follows.

$$K_{ML} = -\frac{1}{T} \ln\left(1 - \frac{1}{\bar{b}}\right), \quad (15)$$

$$\hat{b} = \frac{1}{M} \sum_{i=1}^M b_i. \quad (16)$$

This paper analyzes the time-domain distribution of ocean and ionosphere echoes using the STFT method (e.g., Equation (1)), as depicted in Figure 6.

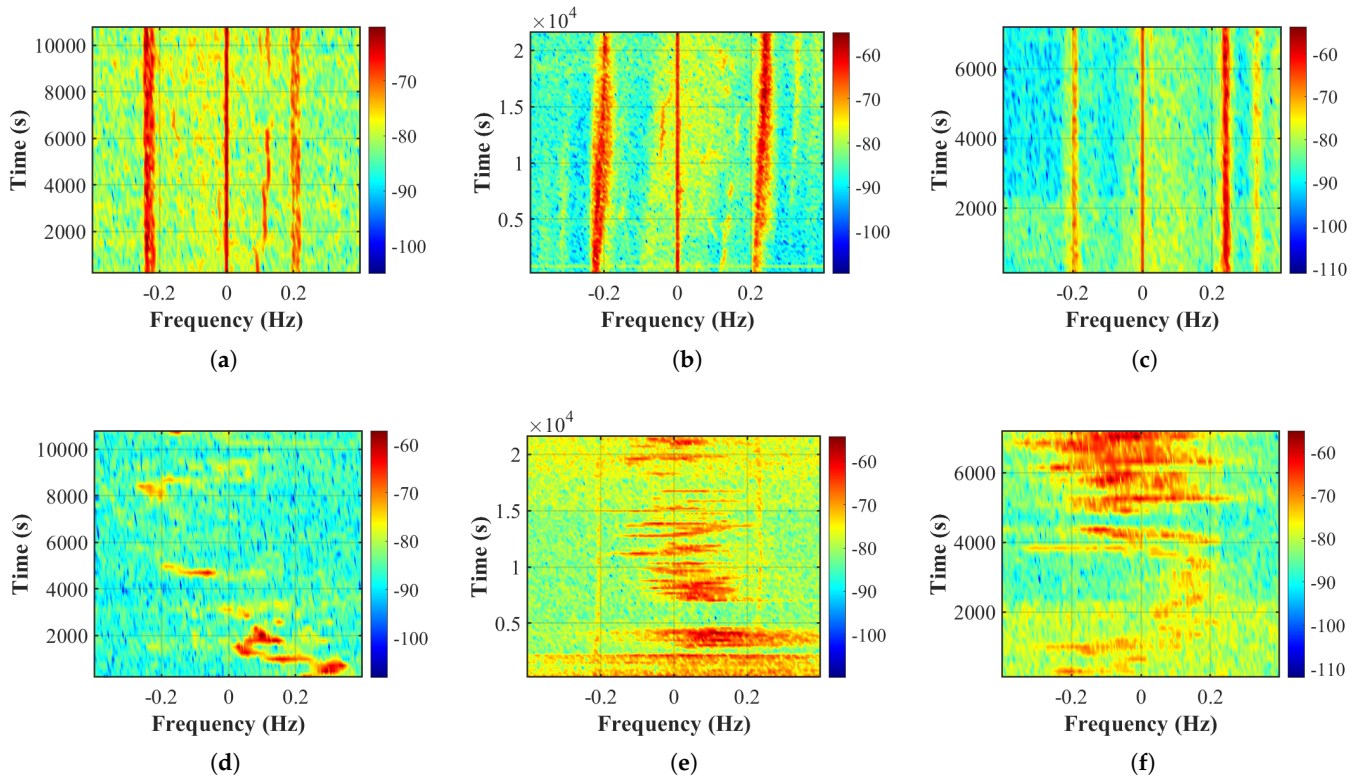


Figure 6. Time–frequency distribution of ocean and ionosphere echoes during severe Typhoon Muifa. (a) 16 September 02:00–05:00: Time–frequency distribution of ocean echoes at the 46th range bin. (b) 16 September 05:00–13:00: Time–frequency distribution of ocean echoes at the 46th range bin. (c) 16 September 13:00–15:00: Time–frequency distribution of ocean echoes at the 46th range bin. (d) 16 September 02:00–05:00: Time–frequency distribution of ionosphere echoes at the 167th range bin. (e) 16 September 05:00–13:00: Time–frequency distribution of ionosphere echoes at the 130th range bin. (f) 16 September 13:00–15:00: Time–frequency distribution of ionosphere echoes at the 140th range bin.

Figure 6 shows significant changes in the ocean and ionosphere echoes with sampling time for HFSWR. The time–frequency distribution of the first-order spectra of the ocean echoes in the fixed-range bin appears to be normal during the two hours before Typhoon Muifa enters the detection range of the HFSWR Weihai station. The quasi-periodic sinusoidal “S” shape of the TIDs can be observed in the time–frequency distribution of the ionospheric echoes, with a period of approximately 2000 s and a frequency range of 0–0.36 Hz. When Typhoon Muifa is within the detection range of HFSWR Weihai station, the first-order spectra of the oceanic echoes exhibit increased frequency broadening, and noticeable Doppler shifts in the time–frequency distribution. At the same time, the “S”-shaped pattern of TIDs in the time–frequency distribution of ionospheric echoes becomes more continuous, centralized, and uniform, forming a multilevel continuous pattern of TIDs with frequencies ranging from -0.4 to 0.4 Hz and -0.2 to 0.2 Hz. A significant Doppler shift in the first-order spectrum of oceanic echoes disappears after Typhoon Muifa moves out of the detection range of the HFSWR Weihai station. The pattern of multistage continuous TIDs remains, but the overall frequency range shift increases, varying from -0.2 to 0 Hz, then from 0 to 0.2 Hz, then from -0.2 to 0.2 Hz, and finally from -0.3 to 0.3 Hz. When

Typhoon Muifa entered the detection range of HFSWR Weihai station, the time–frequency distribution of the ionospheric echoes showed apparent wave-like disturbances, ranging from high frequency to low frequency.

After analyzing the time–frequency distribution in Figure 6, it can be seen that the changes in HFSWR ocean and ionosphere echoes during Typhoon Muifa are gradual and occur in specific regions. A multilevel continuum of the TIDs morphology (long-time domain feature of TIDs) contains multiple quasi-periodic sinusoidal “S”-shaped TIDs morphologies (short-time domain feature of TIDs), and gradual changes in the short-time domain features produce long-time domain features. This approach utilizes a two-dimensional local modal analysis method [32] to study the properties of gravitational wave patterns. The long-time domain signals of TIDs after STFT processing at the 130th range bin are defined as $X(T, f_0)$, where $f_0 = 0.06$ Hz, as shown in Figure 6e. The time series at a frequency of 0.06 Hz contains the time domain signals of the TIDs in addition to the base noise of the HFSWR. In this case, the chaotic structure and complexity of the time series of the same length at different moments are different.

The period of the short-time domain characteristics of TIDs is about 2000 s, i.e., the time length is 2000 s. This study considers $L = 1000$ and uses $17,920 \times 2$ points with the ocean and ionosphere echoes systems’ area $L * L$, which implies $\Delta x = \Delta y = \Delta t = 1000/17,920 = 0.0558$. For the analysis of the spatial patterns, this study computes first the normalized moment $\Sigma = \langle x^2 + y^2 \rangle - \langle x \rangle^2 - \langle y \rangle^2$ with $|X(t, x, y)|^2$ as the statistical weight. $\Delta = 2|\Sigma - \Sigma_c|^{1/2}$ is a measure for the width of the localized pattern, $\Sigma_c = \frac{2}{3}L^2$. The time-averaged $\langle \Delta \rangle_t$ is used below to present the spatial aspects of the results. The central result we want to report in this paper is shown in Figure 7: a chaotic structure of TIDs localized in two dimensions. The normalized values of $|A(x, y)|$ for two fixed times are depicted using the color code on the right. The irregular behavior and progressive behavior in time are apparent.

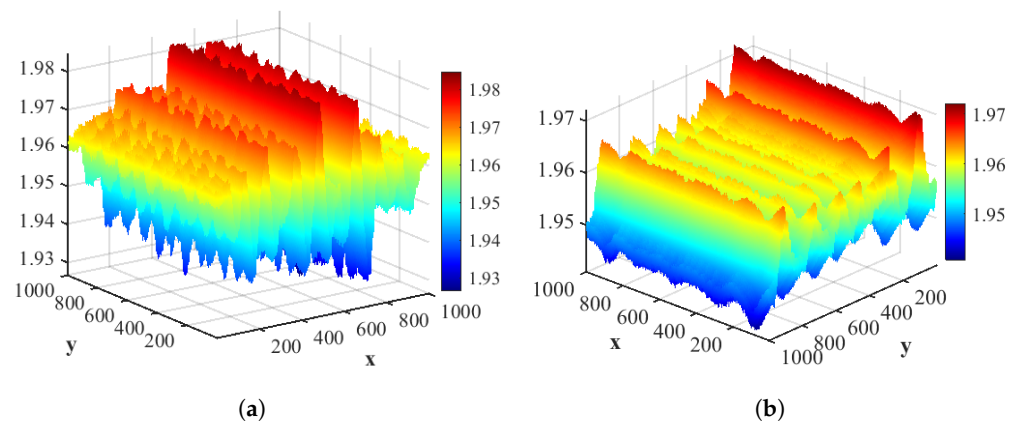


Figure 7. 16 September 05:00–13:00: Chaotic structure in two dimensions of short-time domain feature of TIDs at the 130 range bin during severe Typhoon Muifa. (a) $t = 10,000$ – $12,000$ s; the time-averaged $\langle \Delta \rangle_t$ is 400. (b) $t = 13,000$ – $15,000$ s; the time-averaged $\langle \Delta \rangle_t$ is 180.

To further analyze the gravity wave patterns in HFSWR ocean and ionosphere echoes during severe Typhoon Muifa, this paper extracts the HFSWR ocean and ionosphere echoes’ time series ($X(T, f_0)$) with their gravity wave signature during various typhoon periods and at different time scales. Furthermore, it constructs unique attractors by determining their delay times τ and embedding dimensions m . The obtained phase spaces are as shown in Figure 8. To be more precise, we offer the maximum likelihood estimate of the Kolmogorov entropy K_{ML} in Figure 8.

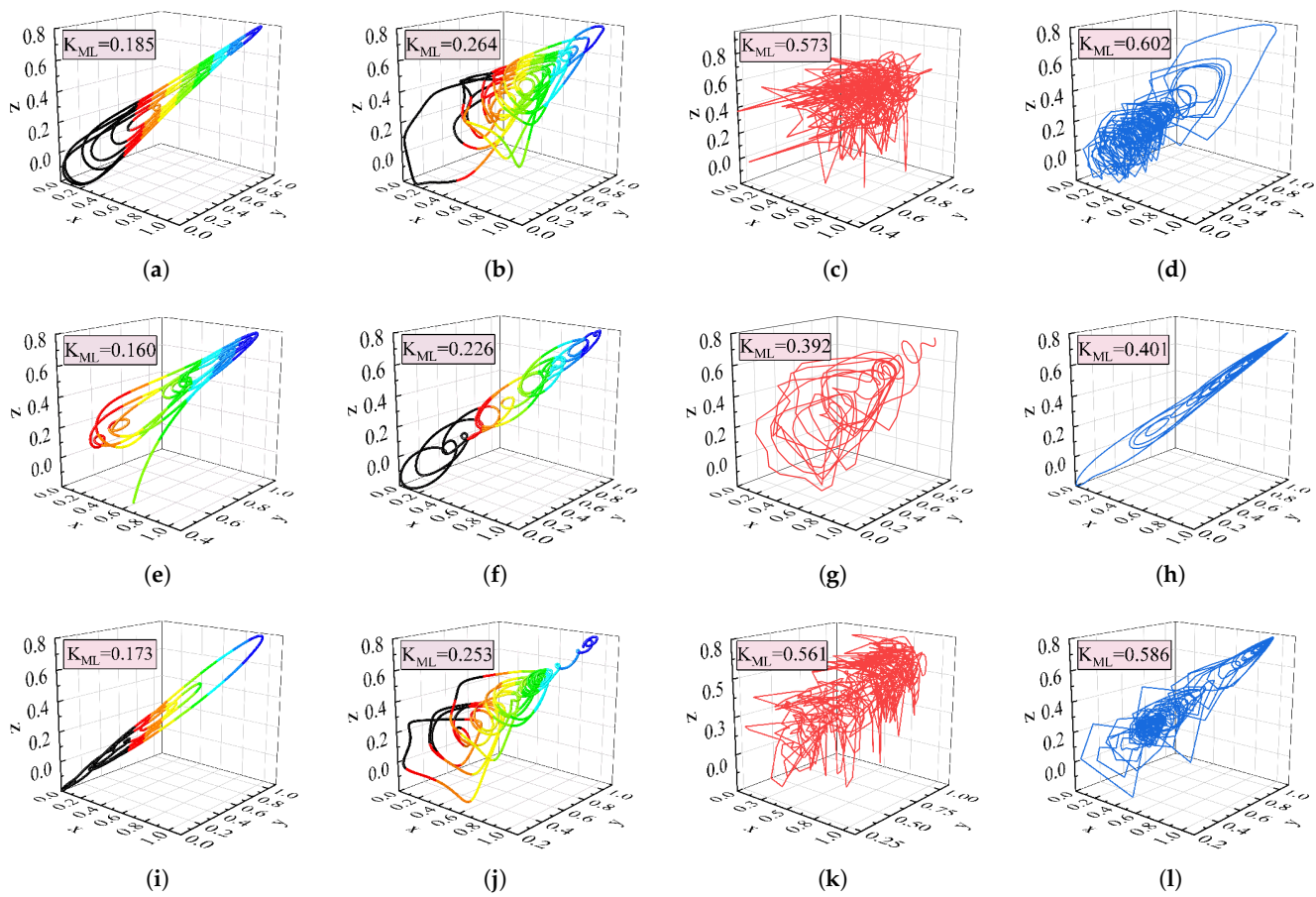


Figure 8. Typical attractor structure (3-D phase portrait) of ocean and ionosphere echoes during severe Typhoon Muifa. (a) 16 September 02:00–05:00: Ocean echoes short-time domain data at the 46th range bin. (b) 16 September 02:00–05:00 Typical TIDs short-time domain data at the 167th range bin. (c) 16 September 02:00–05:00: Ocean echoes long-time domain data at the 46th range bin. (d) 16 September 02:00–05:00: TIDs long-time domain data at the 167th range bin. (e) 16 September 05:00–13:00: Ocean echoes short-time domain data at the 46th range bin. (f) 16 September 05:00–13:00: TIDs short-time domain data at the 130th range bin. (g) 16 September 05:00–13:00: Ocean echoes long-time domain data at the 46th range bin. (h) 16 September 05:00–13:00: TIDs long-time domain data at the 167th range bin. (i) 16 September 13:00–15:00: Ocean echoes short-time domain data at the 46th range bin. (j) 16 September 13:00–15:00: TIDs short-time domain data at the 140th range bin. (k) 16 September 13:00–15:00: ocean echoes long-time domain data at the 46th range bin. (l) 16 September 13:00–15:00: TIDs long-time domain data at the 140th range bin.

Overall, the singular attractors constructed using long-time domain data of TIDs and ocean echoes during typhoons are more disordered in morphology than those of short-time domain data. Noticeably, the ocean echo has similar long-time and short-time domain attractor morphology (Figure 8g,e), as do the TIDs (Figure 8h,f). The above indicates that the singular attractors of the ocean echo or TIDs in the long-time and short-time domain data are only in different evolutionary states, and their long-time and short-time domain characteristics are highly correlated. In addition, describing the singular attractor in the short-time domain is more straightforward than in the long-time domain. TIDs evolve similarly to the typical attractors of ocean echoes, combining the attractor structure and the maximum likelihood estimate of Kolmogorov entropy K_{ML} in Figure 8. As the typhoon center approaches the radar, the attraction between the singular attractor orbits strengthens, resulting in a more regular and uniform singular attractor. Conversely, when the typhoon center moves away from the radar, the attraction between the singular

attractor orbits becomes weaker, causing the singular attractor to disperse outwardly. The typhoon's attractor structure, which is detectable within the HFSSWR range, appears to be in a transition state from complexity to simplicity. Further investigation is needed to determine if typhoons contribute to the regularity of the attractor structure of ocean and ionosphere echoes and how the intrinsic motion mechanism of gravity waves affects the attractor structure of ocean and ionosphere echoes.

Two validation schemes are designed in this paper to increase the generality and reliability of the above characteristics and analysis. Validation scheme 1 focuses on the long- and short-time domain features of TIDs during severe Typhoon Muifa. The experimental data are the long-time domain signals of the TIDs between 05:00 and 13:00. The time duration of the long-time domain signals of the TIDs is 6 h. The short-time domain data are selected from the period 2:00–5:00, and a batch of short-time domain data is about 2000 s.

After processing using the STFT method, the attractor structures are constructed by selecting the time signals at a fixed frequency f_{01} . Figure 9 shows the overall flow and results of validation scheme 1.

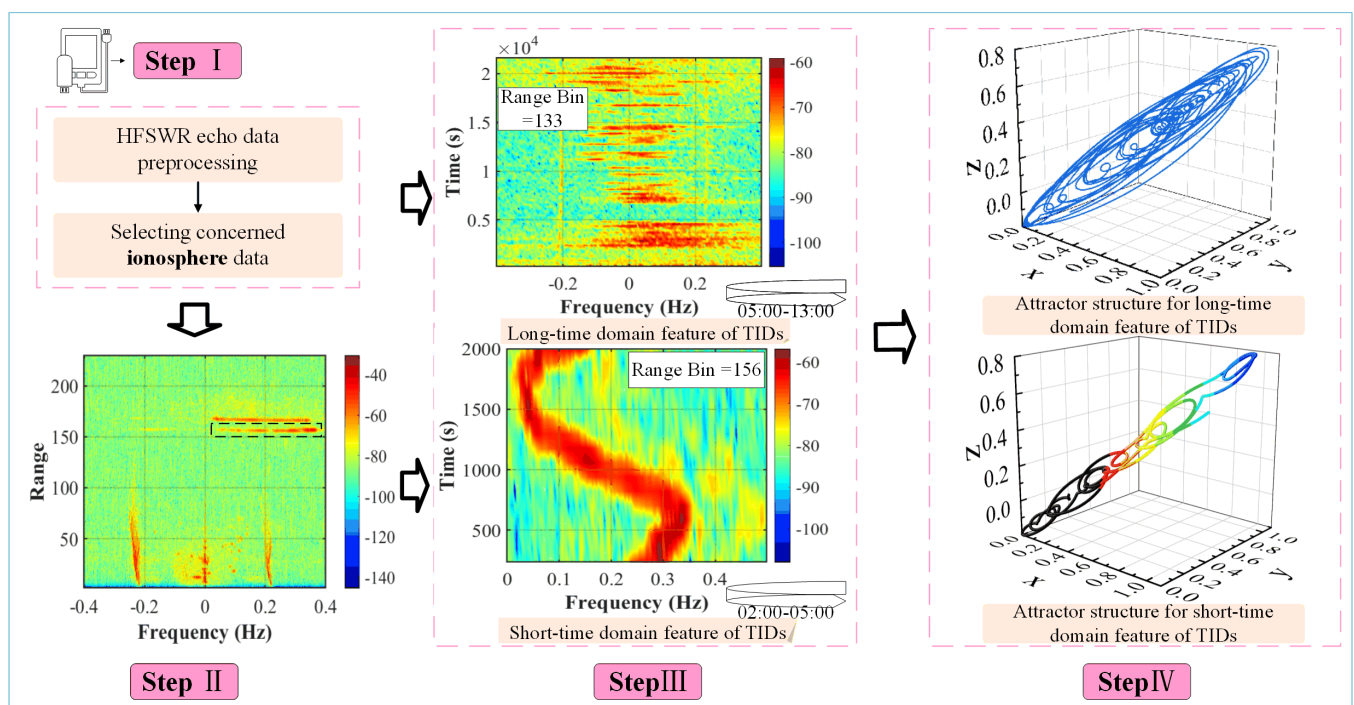


Figure 9. Flowchart and results of validation scheme 1 (TIDs). Note: $f_{011} = 0.06$ Hz, $f_{012} = 0.2$ Hz.

Validation scheme 2 focuses on validating the coupled attractor structure of HFSWR ocean and ionosphere echoes with gravity wave characteristics in the long-time domain under the influence of Typhoon Muifa. The long-domain signals of ocean and ionosphere echoes between 05:00 and 13:00 are selected as the experimental data in validation scheme 2. Note that the period of validation scheme 2 differs from that of validation scheme 1. After processing by the STFT method, the attractor structures of ocean–ionosphere echoes are constructed by selecting the time signals at a fixed frequency f_{02} . Figure 10 shows the overall flow and results of validation scheme 2.

As shown in Figure 9, the time–frequency distribution for the long- and short-time domain features of TIDs in step III are similar to those of TIDs at the 130th range bin in Figure 6e; the attractor structures for long- and short-time domain features of TIDs in step IV are analogous to those of TIDs at the 130th range bin in Figure 8h,f. In Figure 9, using the STFT method, it is possible to extract the long-time domain features of the HFSWR ocean–ionosphere echoes with the joint gravity wave signatures, as shown in step III. Due to the different extraction frequencies, the first-order spectral information of the oceanic echo is present at all sampling points at -0.23 Hz, similar to that at -0.2 Hz during the

02:00–05:00 time period in Figure 6a. The long-time domain attractor structure of the ocean echo in step IV of Figure 10 is thus similar to Figure 8g. This experiment further validates the correlation between HFSWR ocean and ionosphere echoes characterized by gravity wave features.

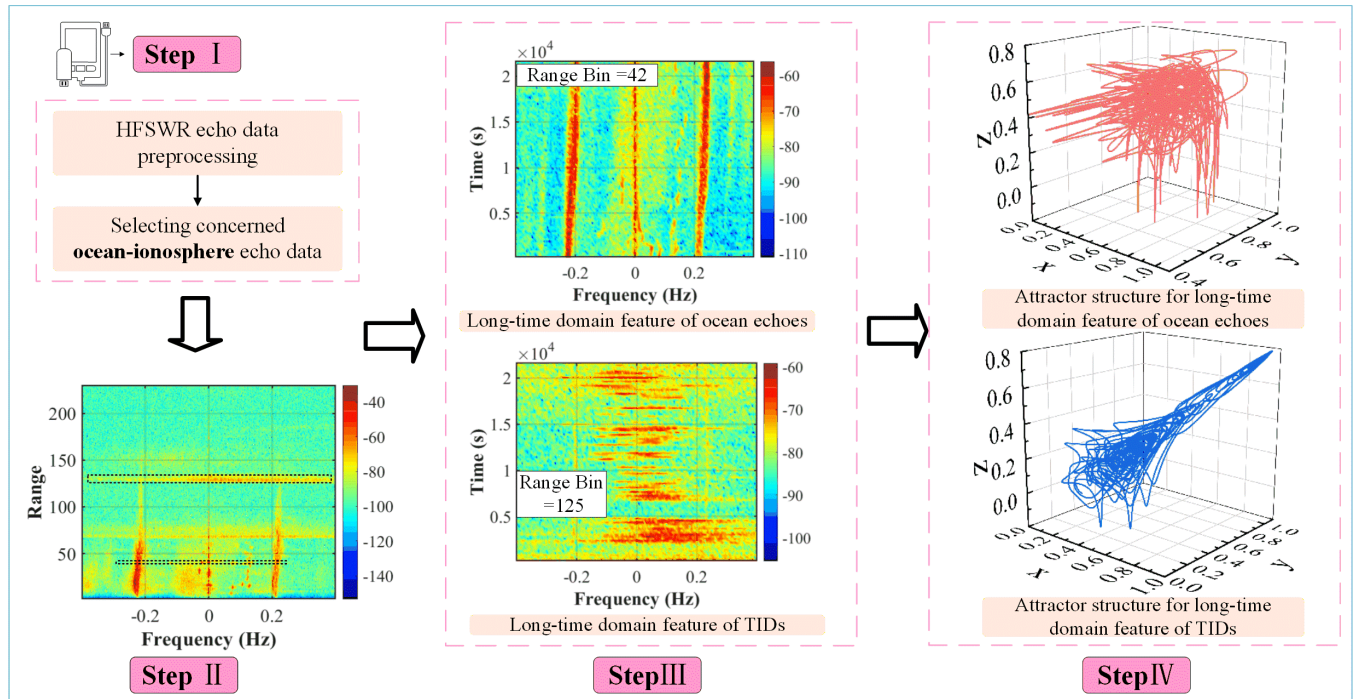


Figure 10. Flowchart and the results of validation scheme 2 (16 September 05:00–13:00). Note: $f_{021} = -0.23$ Hz, $f_{022} = -0.06$ Hz.

3.2. Chaotic Characterization of HFSWR Ocean and Ionosphere Echoes

Section 3.1 employs different methods to analyze the dynamical properties of the ocean and ionosphere hybrid system qualitatively during severe Typhoon Muifa. The universality of the novel proposed ocean and ionosphere echoes' properties during typhoons is verified using additional HFSWR echo data. This section analyzes the chaotic behavior changes of HFSWR ocean and ionospheric echoes during the same period using the maximum Lyapunov exponent. Subsequently, combining their time–frequency distribution characteristics, a preliminary method for characterizing the chaotic behavior of HFSWR ocean and ionospheric echoes during typhoons is summarized. The specific content of this method is summarized as follows:

- Extraction of long-term domain signals: Perform time–frequency preprocessing to obtain the time–frequency distribution of ocean and ionospheric echoes, and then perform frequency sampling to obtain the long-term domain signals of ocean and ionospheric echoes at different frequencies.
- Analysis of chaotic dynamic behavior: Extract continuous short-time domain signals from the long-term domain signals and calculate their maximum Lyapunov exponent. Obtain the time series of the maximum Lyapunov exponent in the long-term domain signals at different sampling frequencies for the analysis of the chaotic dynamic behavior of ocean and ionospheric echoes.
- Characterization of chaotic dynamics: Furthermore, based on the time series of the maximum Lyapunov exponent in the long-term domain signals, extract the chaotic critical points of HFSWR ocean and ionospheric echoes, i.e., the frequencies and sampling moments of HFSWR echoes when chaos occurs, and obtain the two-dimensional chaotic characterization of chaotic critical points at different frequencies.

The largest Lyapunov exponent (LLE_{\max}) [33] gives a quantitative description of the dynamics and is expressed as

$$LLE_{\max} = \lim_{t \rightarrow \infty} \frac{1}{t} \ln \frac{\|\delta_s(t)\|}{\|\delta_s(t_0)\|}, \quad (17)$$

where $\|\bullet\| \equiv (\sum_{i=1}^n (\bullet)_i^2)^{1/2}$, δ_s is a four-dimensional vector, $\frac{\partial \delta_s}{\partial t} = \bar{J} \cdot \delta_s$, \bar{J} represents the Jacobian matrix of the external signal. The numerical value LLE_{\max} quantifies the rate of disappearance ($LLE_{\max} < 0$) or exponential divergence ($LLE_{\max} > 0$) of the distance δs between two initially approaching trajectory points of the field s , the latter being a sign of chaotic behavior.

Euclidean distance characterizing any point (x,y) in the image to the starting point $(0,0)$ is [34],

$$d_0 = \sqrt{x^2 + y^2}. \quad (18)$$

3.2.1. Analysis of Chaotic Dynamic Behavior

This experiment uses data from every 2000 s between 5:00 and 13:00 on 16 September as a batch of short-time domain data. After STFT, the short-time domain signals in the long-time domain with fixed frequencies are selected to obtain $LLE_{i\max}$ (Figure 11), respectively, to study the gravity wave signature of HFSWR ocean–ionospheric echoes during typhoon arrival quantitatively. The selected time-domain signal $S(T) = S(T, f_i), i = 1, 2, \dots, N$ at the frequency (frequency 1 = −0.2 Hz) where the ocean echoes are located and the frequency (frequency 2 = −0.06 Hz) where the TIDs are located; N denotes the number of frequency dimensions after STFT. The sampling moments are normalized to 0–18 and described mathematically as follows:

$$S = \frac{(S_{\max} - S_{\min})(T - T_{\min})}{T_{\max} - T_{\min}} + S_{\min}, \quad (19)$$

where T denotes the sampling time, T_{\max} is the maximum value of T , T_{\min} is the minimum value of T , S denotes the normalized data, S_{\max} is the normalized maximum value, and S_{\min} is the normalized minimum value.

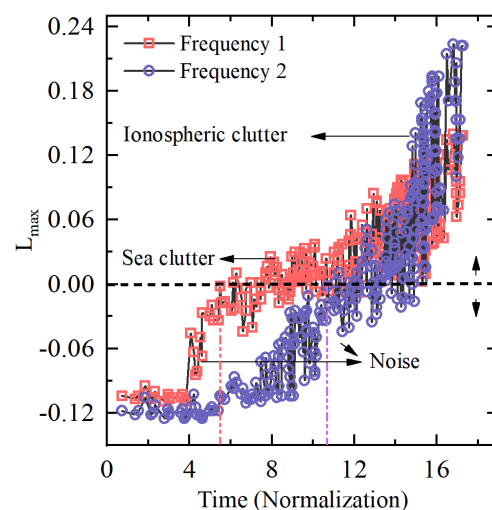


Figure 11. 16 September 05:00–13:00: LLE_{\max} for continuous short-time domain data of ocean–ionosphere echoes during severe Typhoon Muifa.

In Figure 11, the HFSWR ocean and ionosphere echoes with joint gravity wave features transition from a non-chaotic state to a chaotic state at their respective fixed frequencies as the number of samples increases. The ocean echoes precede the traveling ionospheric

disturbances to produce chaotic behavior. Nevertheless, the chaotic variation in the ocean echoes is smoother and eventually reaches a lower level of chaos than the ionospheric echoes. The course of LLE_{\max} in Figure 11 with sampling moments is consistent with the evolution of its time–frequency distribution. The experimental results confirm that LLE_{\max} can well characterize the chaotic properties and evolution of the HFSWR ocean–ionosphere echoes.

3.2.2. Characterization of Chaotic Dynamics

Further, the chaotic threshold of the ocean and ionosphere echoes' evolution process in each batch of data is extracted and the frequency f and the normalized sampling moment T of the chaotic threshold obtained. This experiment selects the short-time domain data among the long-time domain data from 5:00 to 13:00 on 16 September at specific frequencies, as shown in Figure 12. The specific frequencies refer to $f = -0.01 \text{ Hz:d1:0.38 Hz}$, $d1 = 0.04 \text{ Hz}$. This batch of short-time domain data has a duration of 2000 s. This experiment divides a batch of short-time domain data into 18 equal parts and extracts the respective chaotic critical points (f, T) after calculating their LLE_{\max} , as shown in Figure 13. No chaotic and initial chaotic behaviors are normal phenomena in this experiment, so there is no need to reflect them. No chaotic behavior is recorded as 0, and initial chaotic behavior is recorded as 1.

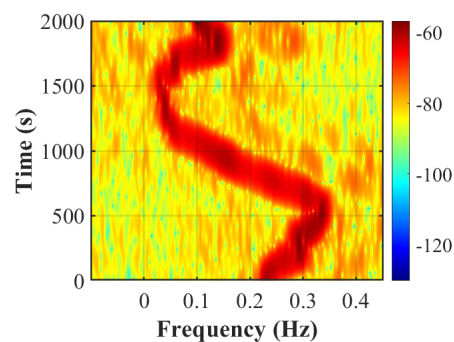


Figure 12. 16 September 02:00–05:00: Short-time domain feature of TIDs.

Figure 13 shows a complete S-shape obtained using FFT by low-pass filtering the chaotic characterization extracted in Figure 12. The above method can effectively characterize the distinct wave-like perturbations that appear in the time–frequency distribution of TIDs, with a frequency span of about 0.36 Hz. Naturally, the chaotic characterization of the long-time domain features of TIDs can be obtained by successively performing chaotic characterization of the short-time domain features of TIDs. It has been shown that the chaotic characterization of the short-time domain features of TIDs for other periods are highly similar to those of Figure 13 and will not be described too much here.

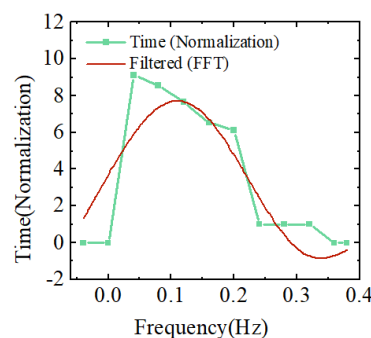


Figure 13. 16 September 02:00–05:00: Chaotic characterization of TIDs in the short-time domain.

It is relatively simple to extract chaotic characterization of the apparent Doppler shift and spreading features of the HFSWR oceanic echoes. The HFSWR ocean echo data (see Figure 6b) in the long-time domain from 5:00 to 13:00 on 16 September is used as the experimental data, with a specific frequency interval $f = -0.28 \text{ Hz:d2}:-0.16 \text{ Hz}$, $d2 = 0.01 \text{ Hz}$, and a time length of 6 h. This experiment calculates the LLE_{\max} once every 2000 s, and then, extracts the respective chaos critical points (f, T) , the results of which are shown in Figure 14. For comparison with HFSWR oceanic echoes under normal conditions, the HFSWR ocean echo data (see Figure 6c) in the long-time domain from 16 September 05:00–13:00 is used as the experimental data, with a specific frequency interval $f = -0.23 \text{ Hz:d2}:-0.17 \text{ Hz}$, $d2 = 0.01 \text{ Hz}$, and a time length of 2 h. This experiment calculates the LLE_{\max} once every 2000 s, and then, extracts the respective chaos critical points (f, T) , the results of which are shown in Figure 15.

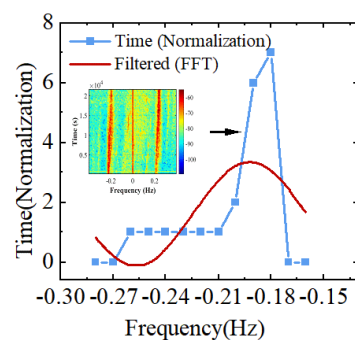


Figure 14. 16 September 05:00–13:00: Chaotic characterization of HFSWR ocean echoes with gravity wave signature.

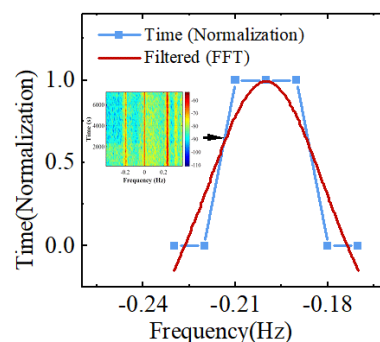


Figure 15. 16 September 02:00–05:00: Chaotic characterization of HFSWR ocean echoes without gravity wave signature.

The experimental results demonstrate that the two-dimensional chaotic representation of chaotic critical points at different frequencies can effectively depict the time–frequency distribution characteristics of HFSWR ocean and ionospheric echoes under typhoon.

3.3. Novel Proposed Characterization Method of HFSWR Ocean and Ionosphere Echoes with Gravity Wave Features during Severe Typhoon Muifa

This paper uses the Euclidean distance as a quantitative criterion for the ocean and ionosphere time–frequency characterization during severe Typhoon Muifa. The gravity wave features of the HFSWR ocean and ionosphere echoes are summarized as follows:

1. The long-time domain feature of ocean echoes (a clear, slightly S-shaped shift in frequency, termed an HFSWR ocean–ionospheric echo with gravity wave signature). Sampling points at the given frequencies need to be significantly Doppler-shifted to match the features of this class. This type of feature occurs when the typhoon is in the detection range of the HFSWR, as shown in Figure 16.

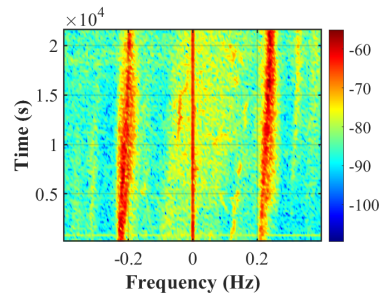


Figure 16. 16 September 05:00–13:00: Long-time domain feature of HFSWR ocean echoes at 46th range bin during severe Typhoon Muifa.

2. Short-time domain feature of TIDs. The short-time domain of TIDs is characterized by a quasi-periodic sinusoidal “S” shape, as shown in Figure 12. The short-time domain feature of TIDs appears before the typhoon enters the detection range of HFSWR, the related research on the short-time domain feature of TIDs may have a positive impact on HFSWR typhoon detection and early warning..
3. Long-time domain feature of TIDs. The long-time domain features of TIDs are in the form of multilevel continuous TIDs, consisting of multiple short-time domain features of TIDs, which appear when the typhoon is within the detection range of the HFSWR. The specific pattern is shown in Figure 17.

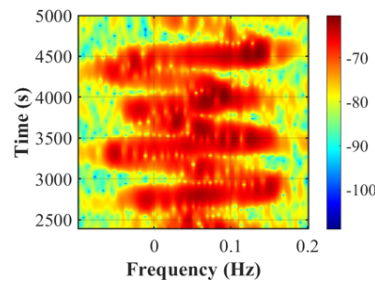


Figure 17. 16 September 05:00–13:00: Short-time domain feature of TIDs at 130 range bin during severe Typhoon Muifa.

The novel proposed characterization method is illustrated with the above three types of HFSWR 46th morphologies with gravity wave characteristics, as shown in Figure 18. The largest Lyapunov exponent of the continuous short-time domain signals in the long-time domain are calculated at different frequencies f , as shown in Figure 11. The critical point $(f_j, Time_j)$ for generating chaotic behavior is recorded; j indicates the number of selected frequencies, as shown in Figure 14. No chaotic behavior is recorded as $Time=0$, and initial chaotic behavior is recorded as $Time=1$. The previous critical point where first $Time \neq 0$ is noted as $(f_{n-1}, Time_{n-1})$, the point at which $Time$ reverts to 0 is denoted as $(f_m, Time_m)$. Assume that the frequency spans of the above three types of gravity wave features are F_1 , F_2 , and F_3 .

1. If there exists $\text{dist}((f_{n-1}, Time_{n-1}), (f_m, Time_m)) = F_3 \pm d1$, then it is the long-time domain feature of the TIDs at that range bin.
2. If there exists $\text{dist}((f_{n-1}, Time_{n-1}), (f_m, Time_m)) = F_2 \pm d2$, then it is the short-time domain feature of the TIDs at that range bin.
3. If there exists $\text{dist}((f_{n-1}, Time_{n-1}), (f_m, Time_m)) > 1$, then it is the long-time domain feature of the sea echoes at that range bin.

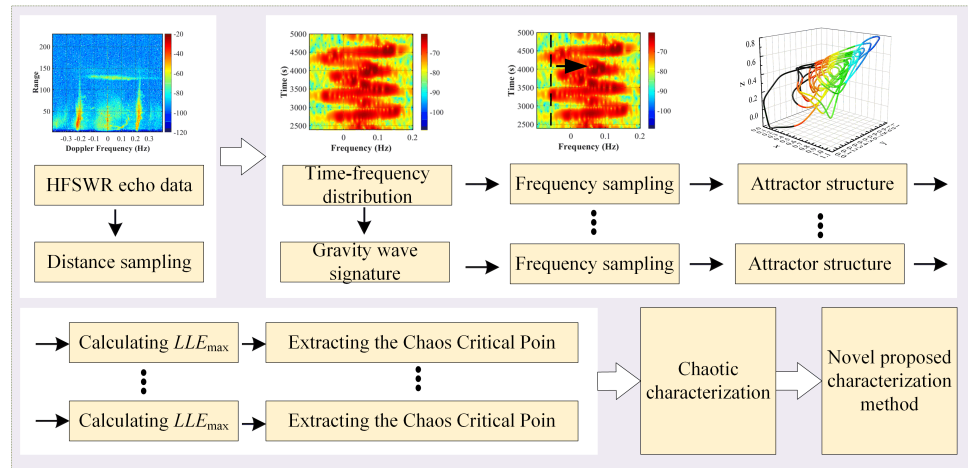


Figure 18. Flowchart of the novel proposed characterization method.

Since $Time_{n-1} = Time_m = 0$, the morphological characterization method quantifies the frequency shift characteristics of the ocean–ionosphere during severe Typhoon Muifa in combination with the Minkowski distance based on extracting chaotic critical points. The morphological characterization method is based on facts and theory. The frequency span is known, and this method can identify the gravity wave signature of HFSWR ocean and ionosphere echoes. The frequency span is unknown, and this method can detect the gravity wave signature of HFSWR ocean and ionosphere echoes, as shown in Figure 19. After processing using the STFT method, the chaotic characterizations are displayed in step IV of Figure 19 by calculating the largest Lyapunov exponents for continuous short-time domain features of ocean and ionosphere echoes at a fixed frequency f_j . As shown in Figure 19, the frequency span of the long-time domain feature of the ocean echoes is detected as 0.06 Hz, and the short-time domain feature of the TIDs is detected as 0.64 Hz, which is accurate.

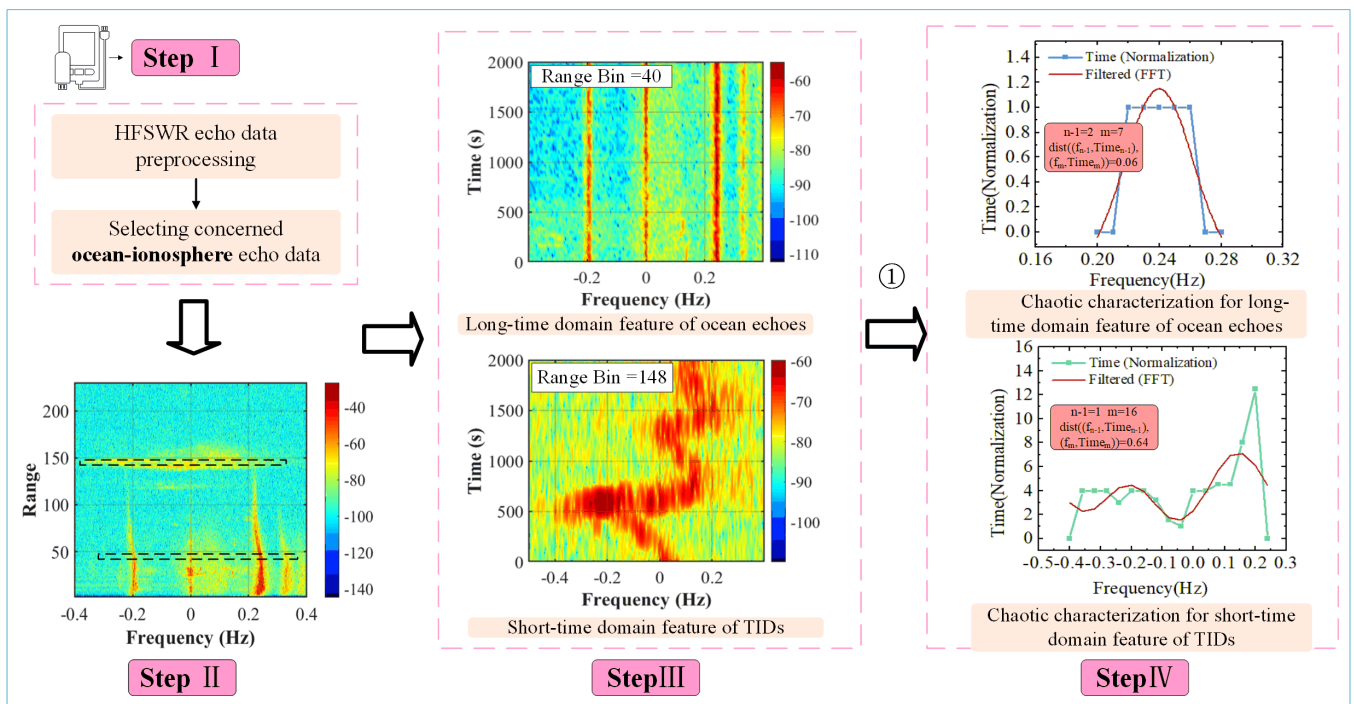


Figure 19. Flowchart and the results of the frequency span detection scheme (16 September 13:00–15:00).

4. Conclusions

This manuscript delineates the identification of HFSWR ocean and ionosphere echoes displaying a joint gravity wave signature, influenced by typhoons. Furthermore, it introduces a novel characterization method for gravity wave signatures in high-frequency surface wave radar (HFSWR), aimed at elucidating the complex interplay between the ocean and the ionosphere during typhoons. The evolution of ocean and ionosphere echoes is analyzed from the time–frequency perspective by the short-time Fourier transform (STFT) method, which confirms the existence of traveling ionospheric disturbances (TIDs) excited by typhoon-induced gravity waves in the ionospheric echoes during typhoons, as well as the presence of apparent weak S-shaped shifts in the ocean echoes in the long-time domain. The ocean and ionosphere echoes have a linkage effect in the abrupt sea state, and the short-time domain feature of the TIDs appears much earlier than the long-time domain feature of the ocean echoes. The dynamics of the ocean and ionosphere echoes during the typhoon are pictorially described using the phase-space reconstruction method with chaotic attractors. This paper proposes a chaotic characterization method to characterize the morphological and chaotic degree of gravity wave signatures, and finally, extracts the long- and short-time domain characteristics of TIDs using HFSWR during Typhoon Muifa, as well as the obvious weak S-shaped offset characteristics of the ocean echoes. In this case, the short-time domain feature of the TIDs is found before the long-time domain feature of the ocean and ionosphere echoes during typhoons. The short-time domain features of TIDs first appear before the typhoon enters the detection range of HFSWR. Applying the short-time domain features of the TIDs combined with the long-time domain features of the ocean and ionosphere echoes to typhoon warnings shows great promise. Experimental validation demonstrates the efficacy of the novel proposed characterization method and the chaotic nature of gravity wave signatures in ocean and ionosphere echoes during intense maritime events. This facilitates not only the classification and detection of HFSWR echoes but also provides insights into the attributes of the HFSWR ocean and ionosphere echoes.

Consequently, this approach introduces an innovative perspective and furnishes robust technical backing to the domain of HFSWR ocean–ionosphere research during severe maritime occurrences. It is essential to note that this contribution represents an initial foray into the intricate dynamics of the HFSWR ocean and ionosphere echoes, warranting further detailed and holistic investigations. Future research directions are as follows:

1. Further refining the characterization methods for HFSWR oceanic and ionospheric echoes during typhoon events.
2. Developing a two-dimensional model for HFSWR oceanic and ionospheric echoes based on the chaotic characteristics observed during typhoon events.
3. Additionally, establishing a joint cancellation model for HFSWR oceanic and ionospheric echoes using control methods.

Author Contributions: Conceptualization, R.W. and Z.L.; methodology, R.W.; software, R.W.; validation, C.Y., Z.L., A.L. and T.Q.; formal analysis, Z.L.; investigation, R.W.; resources, C.Y.; data curation, C.Y., R.W. and A.L.; writing—original draft preparation, R.W.; writing—review and editing, R.W. and C.Y.; visualization, R.W.; supervision, C.Y., Z.L., A.L. and T.Q.; project administration, C.Y.; funding acquisition, C.Y. and A.L. All authors have read and agreed to the published version of the manuscript.

Funding: This work was supported in part by the National Natural Science Foundation of China under Grant 62031015, and Mount Taishan Scholar Distinguished Expert Plan 20190957, and Natural Science Foundation of Shandong Province under Grant ZR2023QF118.

Data Availability Statement: Data are contained within the article.

Conflicts of Interest: The authors declare no conflicts of interest.

Abbreviations

The following abbreviations are used in this manuscript:

HFSWR	High-frequency surface wave radar
STFT	Short-time Fourier transform
TIDs	Traveling ionospheric disturbances
LLE_{\max}	Largest Lyapunov exponents
RD	Range-Doppler

References

- Nemchinov, I.V.; Zetzer, Y.I.; Kovalev, A.T.; Shuvalov, V.V. Perturbations in the ionosphere and magnetosphere during the fall of cosmic bodies onto land or ocean. *Dokl. Earth Sci.* **2006**, *409*, 736–738. [[CrossRef](#)]
- Lee, S.M. A Far Field Solution of the Slowly Varying Drift Force on an Offshore Structure in Bichromatic Waves—Two Dimensional Problems. *J. Ocean. Eng. Technol.* **2008**, *2*, 7–12.
- Isaev, N.V.; Chmyrev, V.M.; Serebryakova, O.N.; Yushchenko, A.K. Disturbance of the Electric Field in the Ionosphere by Sea Storms and Typhoons. *Cosm. Res.* **2002**, *40*, 547–553. [[CrossRef](#)]
- Sorokin, V.M.; Isaev, N.V.; Yaschenko, A.K.; Chmyrev, V.M.; Hayakawa, M. Strong DC electric field formation in the low latitude ionosphere over typhoons. *J. Atmos. Sol.-Terr. Phys.* **2002**, *67*, 1269–1279. [[CrossRef](#)]
- Hines, C.O. Internal atmospheric gravity waves at ionospheric heights. *Can. J. Phys.* **1960**, *38*, 1424–1427. [[CrossRef](#)]
- Xiao, G.; Hao, Y.; Zhang, D.; Xiao, Z. A case study on whole response processes of the ionosphere to typhoons. *Chin. J. Geophys.* **2006**, *49*, 623–628. [[CrossRef](#)]
- Xiao, G.; Zhang, D.; Xiao, Z. Study on the detectability of typhoon-generated acoustic-gravity waves. *Chin. J. Space Sci.* **2007**, *27*, 35–40. [[CrossRef](#)]
- Yang, X.G. Research on Ionospheric Echo Mechanism and Application of High-Frequency Surface Wave Radar. Doctoral Dissertation, Harbin Institute of Technology, Harbin, China, 2019.
- Collinson, G.; Fadden, J.M.; Mitchell, D.; Grebowsky, J.; Benna, M.; Espley, J.; Jakosky, B. Traveling Ionospheric Disturbances at Mars. *Geophys. Res. Lett.* **2019**, *46*, 4554–4563. [[CrossRef](#)]
- Yang, Z.; Zhou, H.; Tian, Y.; Huang, W.; Shen, W. Improving Ship Detection in Clutter-Edge and Multi-Target Scenarios for High-Frequency Radar. *Remote Sens.* **2021**, *13*, 4305. [[CrossRef](#)]
- Sun, W.; Huang, W.; Ji, Y.; Dai, Y.; Ren, P.; Zhou, P.; Hao, X. A Vessel Azimuth and Course Joint Re-Estimation Method for Compact HFSWR. *IEEE Trans. Geosci. Remote Sens.* **2020**, *58*, 1041–1051. [[CrossRef](#)]
- Sun, W.; Li, X.; Pang, Z.; Ji, Y.; Dai, Y.; Huang, W. Track-to-Track Association Based on Maximum Likelihood Estimation for T/R-R Composite Compact HFSWR. *IEEE Trans. Geosci. Remote Sens.* **2023**, *61*, 1–12. [[CrossRef](#)]
- Zhao, C.; Deng, M.; Chen, Z.; Ding, F.; Huang, W. Ocean Wave Parameters and Nondirectional Spectrum Measurements Using Multifrequency HF Radar. *IEEE Trans. Geosci. Remote Sens.* **2022**, *13*, 1–13. [[CrossRef](#)]
- Chen, Z.; Chen, X.; Zhao, C.; Li, J.; Huang, W.; Gill, E.W. Observation and Intercomparison of Wave Motion and Wave Measurement Using Shore-Based Coherent Microwave Radar and HF Radar. *IEEE Trans. Geosci. Remote Sens.* **2019**, *57*, 7594–7605. [[CrossRef](#)]
- Huang, W.; Gill, E.; Wu, X.; Li, L. Measurement of Sea Surface Wind Direction Using Bistatic High-Frequency Radar. *IEEE Trans. Geosci. Remote Sens.* **2012**, *50*, 4117–4122. [[CrossRef](#)]
- Huang, W.; Carrasco, R.; Shen, C.; Gill, E.W.; Horstmann, J. Surface Current Measurements Using X-Band Marine Radar with Vertical Polarization. *IEEE Trans. Geosci. Remote Sens.* **2016**, *54*, 2988–2997. [[CrossRef](#)]
- Walsh, J.; Chen, S.; Gill, E.; Huang, W. High frequency radar clutter power for mixed ionosphere-ocean propagation. In Proceedings of the 2014 16th International Symposium on Antenna Technology and Applied Electromagnetics, Victoria, BC, Canada, 13–16 July 2014.
- Walsh, J.; Gill, E.W.; Huang, W.; Chen, S. On the Development of a High-Frequency Radar Cross Section Model for Mixed Path Ionosphere-Ocean Propagation. *IEEE Trans. Antennas Propag.* **2015**, *63*, 2655–2664. [[CrossRef](#)]
- Chen, S.; Huang, W.; Gill, E.W. First-order bistatic high-frequency radar power for mixed-path ionosphere-ocean propagation. *IEEE Geosci. Remote Sens. Lett.* **2016**, *13*, 1940–1944. [[CrossRef](#)]
- Walsh, J.; Huang, W.; Gill, E. The second-order high frequency radar ocean surface cross section for an antenna on a floating platform. *IEEE Trans. Antennas Propag.* **2012**, *60*, 4804–4813. [[CrossRef](#)]
- Chen, S.; Gill, E.W.; Huang, W. A High-Frequency Surface Wave Radar Ionospheric Clutter Model for Mixed-Path Propagation With the Second-Order Sea Scattering. *IEEE Trans. Antennas Propag.* **2016**, *64*, 5373–5381. [[CrossRef](#)]
- Li, Z.; Jia, C.; Huang, D. Research on characteristics of ionospheric echo based on ocean. In Proceedings of the 2016 IEEE Advanced Information Management, Communicates, Electronic and Automation Control Conference (IMCEC), Xian, China, 3–5 October 2016.
- Chung, Y.J.; Chen, H.C.; Chen, Y.R.; Chiao Tsai, S.; Yang, Y.J.; Chuang, L.Z.H. Clutter Analysis of the Range-Doppler Spectra under the Influence of Typhoon. In Proceedings of the OCEANS 2019, Marseille, France, 17–20 June 2019.

24. Zhou, H.; Wen, B.; Wu, S. Ionosphere Probing with a high frequency surface wave radar. *Prog. Electromagn. Res. C* **2011**, *20*, 203–214. [CrossRef]
25. Typhoon Naming List. Available online: [https://baike.baidu.com/reference/61965809/249aq-yVKPZIddilmkCD3P\\$_\\$fWj8GAY6FZUFdKrkJkmLsHuDDalxhHM7t8UIte5wFNCjIruwTEXknt7tMrOzq1W179oH6tJ\\$\protect\discretionary{\char\hyphenchar\font}{}}{\\\$eNm16tamB4hw9n2\\$_\\$fXHo](https://baike.baidu.com/reference/61965809/249aq-yVKPZIddilmkCD3P$_$fWj8GAY6FZUFdKrkJkmLsHuDDalxhHM7t8UIte5wFNCjIruwTEXknt7tMrOzq1W179oH6tJ$\protect\discretionary{\char\hyphenchar\font}{}}{\$eNm16tamB4hw9n2$_$fXHo) (accessed on 27 December 2023).
26. Typhoon Ocean. Available online: [https://baike.baidu.com/reference/61965809/19f7yHPMec-gZ2x0OXjnzUwNVNIL5cbK3h0PX7aKXRAG3lMd7qK9v5H-ub\\$_\\$bkRHYnctec28gJXMNvOWPrHzHe\\$_\\$b-R5pBHvTPzmt5N209Q](https://baike.baidu.com/reference/61965809/19f7yHPMec-gZ2x0OXjnzUwNVNIL5cbK3h0PX7aKXRAG3lMd7qK9v5H-ub$_$bkRHYnctec28gJXMNvOWPrHzHe$_$b-R5pBHvTPzmt5N209Q) (accessed on 27 December 2023).
27. Samden! Typhoon “Muifa” Has Made Landfall in Qingdao as the Latest Typhoon in Shandong. Available online: [https://baike.baidu.com/reference/61965809/5ac9STppICJsUy-27jC8xFNSuSx1NtHumm408RIZaA0YPU-igb6vKxQnaKU8b0yT785cOZIAUXPaNzup\\$_\\$COvxcwqwIwSXgkaBholUMduNWqOjgvTux5NMGSDqY-PNL9oUtm](https://baike.baidu.com/reference/61965809/5ac9STppICJsUy-27jC8xFNSuSx1NtHumm408RIZaA0YPU-igb6vKxQnaKU8b0yT785cOZIAUXPaNzup$_$COvxcwqwIwSXgkaBholUMduNWqOjgvTux5NMGSDqY-PNL9oUtm) (accessed on 27 December 2023).
28. Pilipovic, S.; Prangoski, B. On the Characterizations of Wave Front Sets in Terms of the Short-Time Fourier Transform. *Math. Notes* **1019**, *105*, 153–157. [CrossRef]
29. Crutchfield, J.P.; Farmer, J.D.; Packard, N.H.; Shaw, R.S. Chaos. *Sci. Am.* **1986**, *254*, 46–57. [CrossRef]
30. Kennel, M.B.; Brown, R.; Abarbanel, H. Determining embedding dimension for phase-space reconstruction using a geometrical construction. *Am. Phys. Soc.* **1992**, *45*, 3403–3411. [CrossRef] [PubMed]
31. Schouten, J.C.; Takens, F.; Bleek, C. Maximum-likelihood estimation of the entropy of an attractor. *Phys. Rev. E* **1994**, *49*, 126–129. [CrossRef]
32. Urzagasti, D.; Laroze, D.; Pleiner, H. Two-dimensional localized chaotic patterns in parametrically driven systems. *Phys. Rev. E* **2017**, *95*, 052216. [CrossRef]
33. Aurell, E.; Boffetta, G.; Crisanti, A.; Paladin, G.; Vulpian, A. Predictability in the large: An extension of the concept of Lyapunov exponent. *J. Phys. A Math. Gen.* **1996**, *30*, 1–26. [CrossRef]
34. Cao, S.; Li, H.; Zhang, K.; Yang, C.; Sun, F.; Wang, Z. An improved chaotic recognition method for weak signal frequency and its application to fault diagnosis of planetary gearboxes. *Meas. Sci. Technol.* **2016**, *33*, 105113. [CrossRef]

Disclaimer/Publisher’s Note: The statements, opinions and data contained in all publications are solely those of the individual author(s) and contributor(s) and not of MDPI and/or the editor(s). MDPI and/or the editor(s) disclaim responsibility for any injury to people or property resulting from any ideas, methods, instructions or products referred to in the content.